

Method and Apparatus for Precisely Applying Large Planar Equi-Biaxial Strains to a Circular Membrane

by Geoffrey A. Slipher

ARL-TR-6432

April 2013

NOTICES

Disclaimers

The findings in this report are not to be construed as an official Department of the Army position unless so designated by other authorized documents.

Citation of manufacturer's or trade names does not constitute an official endorsement or approval of the use thereof.

Destroy this report when it is no longer needed. Do not return it to the originator.

Army Research Laboratory

Aberdeen Proving Ground, MD 21005-5066

ARL-TR-6432

April 2013

Method and Apparatus for Precisely Applying Large Planar Equi-Biaxial Strains to a Circular Membrane

Geoffrey A. Slipper
Vehicle Technology Directorate, ARL

REPORT DOCUMENTATION PAGE				Form Approved OMB No. 0704-0188	
Public reporting burden for this collection of information is estimated to average 1 hour per response, including the time for reviewing instructions, searching existing data sources, gathering and maintaining the data needed, and completing and reviewing the collection information. Send comments regarding this burden estimate or any other aspect of this collection of information, including suggestions for reducing the burden, to Department of Defense, Washington Headquarters Services, Directorate for Information Operations and Reports (0704-0188), 1215 Jefferson Davis Highway, Suite 1204, Arlington, VA 22202-4302. Respondents should be aware that notwithstanding any other provision of law, no person shall be subject to any penalty for failing to comply with a collection of information if it does not display a currently valid OMB control number. PLEASE DO NOT RETURN YOUR FORM TO THE ABOVE ADDRESS.					
1. REPORT DATE (DD-MM-YYYY) April 2013		2. REPORT TYPE Final		3. DATES COVERED (From - To) February 2011–February 2013	
4. TITLE AND SUBTITLE Method and Apparatus for Precisely Applying Large Planar Equi-Biaxial Strains to a Circular Membrane				5a. CONTRACT NUMBER	
				5b. GRANT NUMBER	
				5c. PROGRAM ELEMENT NUMBER	
6. AUTHOR(S) Geoffrey A. Slipher				5d. PROJECT NUMBER	
				5e. TASK NUMBER	
				5f. WORK UNIT NUMBER	
7. PERFORMING ORGANIZATION NAME(S) AND ADDRESS(ES) U.S. Army Research Laboratory ATTN: RDRL-VTA Aberdeen Proving Ground, MD 21005-5066				8. PERFORMING ORGANIZATION REPORT NUMBER ARL-TR-6432	
9. SPONSORING/MONITORING AGENCY NAME(S) AND ADDRESS(ES)				10. SPONSOR/MONITOR'S ACRONYM(S)	
				11. SPONSOR/MONITOR'S REPORT NUMBER(S)	
12. DISTRIBUTION/AVAILABILITY STATEMENT Approved for public release; distribution is unlimited.					
13. SUPPLEMENTARY NOTES					
14. ABSTRACT This report describes the design, operation, and performance assessment of an apparatus, whereby a planar equi-biaxial strain may be applied to a circular membrane in a precisely controlled and repeatable manner. The strained state may be held indefinitely to enable the study of mechanical creep and other phenomena while the membrane remains attached to the apparatus. The apparatus is also capable of removing the sample for further experimentation without losing the strained state. Circular area strains may be accurately controlled between 0% and in excess of 600%, with a minimum resolution of 0.003% applied area strain. This report also describes the methodology that was used to design the apparatus as well as an analysis of its performance. Appropriate material samples to be considered using the as-built apparatus described herein are planar circular membranes that have a nominal Young's modulus on the order of tens of megapascals or less and a nominal thickness up to ~1 mm.					
15. SUBJECT TERMS large planar equi-biaxial strain, membrane, dielectric elastomers, electromechanical transducers, stretchable electronics					
16. SECURITY CLASSIFICATION OF:			17. LIMITATION OF ABSTRACT UU	18. NUMBER OF PAGES 30	19a. NAME OF RESPONSIBLE PERSON Geoffrey A. Slipher
a. REPORT Unclassified	b. ABSTRACT Unclassified	c. THIS PAGE Unclassified			19b. TELEPHONE NUMBER (Include area code) 410-278-3654

Contents

List of Figures	iv
Acknowledgments	v
1. Introduction	1
2. Design	2
2.1 Basic Operational Concept.....	3
2.2 Significant Features.....	9
2.2.1 Shaft Encoders.....	10
2.2.2 Clamp Design (Jaw Shape and Screw-Down Method).....	11
2.2.3 Antitwist Cover	11
2.2.4 Electrical Interfaces for In Situ Electrical Characterization.....	13
3. Validation and Performance Assessment	14
3.1 Validation of Uniform Head Displacement.....	14
3.2 Photographic Validation of Applied Strain	15
3.3 Validation of Strain Uniformity Using DIC.....	17
4. Conclusions	18
5. References	20
Distribution List	21

List of Figures

Figure 1. Representative data showing significant nonlinear shifts in electronic properties of a device undergoing large deformation (in this case, equi-biaxial area strain).	2
Figure 2. Basic apparatus components.....	3
Figure 3. Gear track motion for increasing strain (shown at minimum strain, starting position).	4
Figure 4. Spur gear rotation for increasing strain and corresponding clamp head displacement (shown at maximum strain).	4
Figure 5. Comparison of Poisson's effect for eight clamp heads (left) and sixteen clamp heads (right).	5
Figure 6. Apparatus top view including slide mount (ring at center) with significant dimensions and limits called out.....	6
Figure 7. The relationship between desired area strain values and the number of motor steps required to achieve the desired strain is shown for the as-designed apparatus.....	8
Figure 8. The as-built envelope for resolution, assuming microstepping is used.....	9
Figure 9. Primary motor encoder (left) and secondary shaft encoder (right) placements.	10
Figure 10. Upper clamp geometry (highlighted, left) and clamp head assembly showing clamping and handling features (right).	11
Figure 11. Antitwist cover with major features labeled.....	12
Figure 12. Final design embodiment of the apparatus.....	12
Figure 13. Conducting clamp components for electrical interface to a specimen.	13
Figure 14. Two typical configurations for characterizing shift in electrical properties with large biaxial strain: upper clamp jaw configuration for four-wire conductivity measurements (left) and dual upper/lower jaw configuration for measurement of capacitance on a hyperelastic compliant capacitor (right).	13
Figure 15. Representative data of head displacement curve fitting using the laser displacement sensor.	14
Figure 16. Cross-head variability from average displacement slope for each of the 16 heads.....	15
Figure 17. Photo measurement grid.	16
Figure 18. Overlay of photo-measured strain data and predicted strain values vs. number of stepper motor steps.	16
Figure 19. Zoomed in from figure 17, example of worst-case bounds on pixel selection for the centroid of a point (indicated by black dot) in the image-processing algorithm.	17
Figure 20. DIC results showing uniform strain distribution for (from top to bottom) 0%, 150%, and 400% area strains.	18

Acknowledgments

The author gratefully acknowledges the contributions of the following colleagues, without which this work would not have been as successful:

- Mr. Mark Foster (U.S. Army Research Laboratory [ARL]/Weapons and Materials Research Directorate contractor) for his assistance with processing images using the VIC-3-D software.
- Mr. Stephen Biggs (ARL/Vehicle Technology Directorate [VTD] contractor with Motile Robotics) for final component manufacture using the Stratasys FDM 400 3-D printing machine.
- Mr. Christopher Kroninger (ARL/VTD) for his helpful suggestion of using coaxially aligned rods to produce the useful clamp-head motions.
- Mr. Howard Carpenter (ARL/VTD contractor with Bowhead) for valuable design suggestions, valuable, and at times lengthy, design discussions, and for his attention to detail and quality in the manufacture of components using a laser cutter, Objet 3-D printer, lathe, and Haas CNC milling machine.

INTENTIONALLY LEFT BLANK.

1. Introduction

The apparatus described herein was designed and constructed as an aid to the electromechanical characterization of composited soft elastomeric materials subjected to large biaxial deformations. The basic function of the apparatus was inspired by an experiment on pure homogeneous deformation of rubber sheets first described by Treloar (Treloar, 1948) and later modified by Rivlin and Saunders (Rivlin and Saunders, 1997). The U.S. Army Research Laboratory is interested in these elastomers as either dielectric or conducting layers in composited stretchable electromechanical transduction mechanisms. Such composited devices are of interest for actuation and sensing applications in highly compliant survivable systems, such as compliant robotics, stretchable electronic devices, clothing-integrated electronics, Soldier biosensing, and stretchable adaptive antennas. Whereas most material characterizations are performed under uniaxial strain conditions, such tests are not suitable for some emerging applications of potential interest to the Army and Department of Defense—notably, clothing-integrated distributed electronic devices and large-area distributed actuator systems for biologically inspired robotic mobility. In both cases, real-world scenarios dictate that experimentation, modeling, and analysis are more accurate if biaxial stress-strain conditions are considered. Of particular concern are reliability and failure analyses. Uniaxial stress-strain conditions simply cannot create stress conditions arising from multiaxial loads that can lead to earlier failures—in particular, at anisotropic material-material interfaces. Thus, a means of producing biaxial strain and stress in a reliable and repeatable way for research purposes was identified as a requirement in order to evaluate emerging stretchable electronics technologies for potential future Army applications.

Electronic properties, such as dielectric strength, capacitance, resistance, and inductance, vary significantly and nonlinearly when stretchable electronic devices are subjected to large deformations (Jean-Mistral et al., 2010; Slipper et al., 2012). Shifts in dielectric strength and resistance are primarily determined by inherent bulk material properties, including microstructure, while shifts in inductance and capacitance are primarily influenced by changes in device geometry during deformation. Large deformations result in changes in both the material microstructure and the bulk material geometry, thus leading to complex shifts in electrical and mechanical impedances. Figure 1 shows a representative data set that illustrates the significance of shift in electronic behavior with strain for a stretchable capacitor. For example, note the initial increase in capacitance that would be expected for a parallel plate capacitor as the area increases and the dielectric thickness decreases. The resulting change in slope, and then decrease in capacitance, is associated with reaching and then passing the percolation threshold for a localized resistive component as strain is increased. This change reduces the effective area of the capacitor, and thus reduces capacitance, as the charge mobility is eliminated over an increasingly significant area of the capacitor.

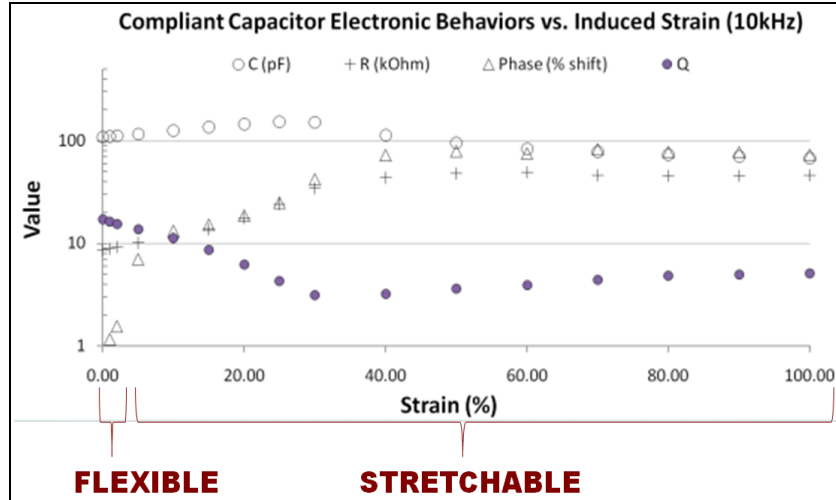


Figure 1. Representative data showing significant nonlinear shifts in electronic properties of a device undergoing large deformation (in this case, equi-biaxial area strain).

Note: The “flexible” electronics and “stretchable” electronics regimes are called out for contextualization and comparison.

Understanding the variation in electronic and mechanical properties with strain is important for both exploitation of such variation (e.g., for sensing applications) and mitigation of, or adaptation to, the variation for effective operation of stretchable electronic devices. For example, impedance matching is critical for designing efficient driving circuitry for AC-driven stretchable actuator systems. However, as the total impedance of the stretchable device changes, the driving circuitry needs to adapt to maintain the same level of efficiency. It is thus important to understand the degree of shift in impedance for a given device over its operating range of frequency and deformation in order to design efficient driving circuitry for it.

Determining the constitutive electronic properties of the material system, in addition to the mechanical properties, is thus a prerequisite for designing highly compliant electronic devices (e.g., highly deformable muscle-like actuators for biologically inspired robotic mobility). The apparatus described herein allows scientists to perform additional experiments to determine the constitutive electronic and mechanical properties of a variety of stretchable electronic materials over a wide range of equi-biaxial strains.

2. Design

The apparatus was designed to give the user a wide range of equi-biaxial straining capability while maintaining repeatability, ease of use, and the ability to remove the sample, if desired, to carry out additional experiments without losing the strained reference state. In anticipation that the apparatus would be used to prepare hundreds of samples, we designed the apparatus for

speed, efficiency of operation, and ease of use. In its final form, the apparatus is operated via computer to allow precise closed-loop control over the desired strain state. We achieved precision by using combination micro-stepping stepper motors, precision ground steel acme threaded rods, and a small clamp head advance ratio of $\sim 0.3 \mu\text{m}$ per motor step ($2.899\text{E-}7 \text{ m}$) with micro-stepping enabled on the motor driver. Without micro-stepping enabled, the advance ratio is $\sim 2.9 \mu\text{m}$ of linear extension of the clamp head per step.

2.1 Basic Operational Concept

The user operates the apparatus by rotating a circular gear track, which simultaneously spins 16 radially aligned spur gear heads. Each spur gear head is coaxially fixed to precision steel acme-threaded rods via a matched precision threaded nut. Sixteen clamping heads are fixed to the inner end of each threaded rod. Clamping heads are used to clamp the outer edge of the membrane that is to be deformed. As the spur gears are spun by the action of rotating the gear track, the threaded rods are advanced radially relative to the clamp heads via the nut. The geometry of the clamp heads restricts the minimum starting radius of the sample. The geometry of the supporting fixture restricts the maximum displacement that can be achieved by the clamp heads. The interplay between these two restrictions is the primary design consideration requiring careful selection of apparatus and component geometry in order to achieve a desired range of strain. Figures 2–4 illustrate the basic form and operation of the apparatus. Figure 2 shows the basic functional components: the gear track, spur gears, threaded rods, and the clamp heads that grip the sample to be strained. Figure 3 shows the rotation of the gear track to advance the clamp heads radially outward and increase strain on the specimen. Figure 4 shows the corresponding spur gear rotation and clamp head displacement at maximum strain.

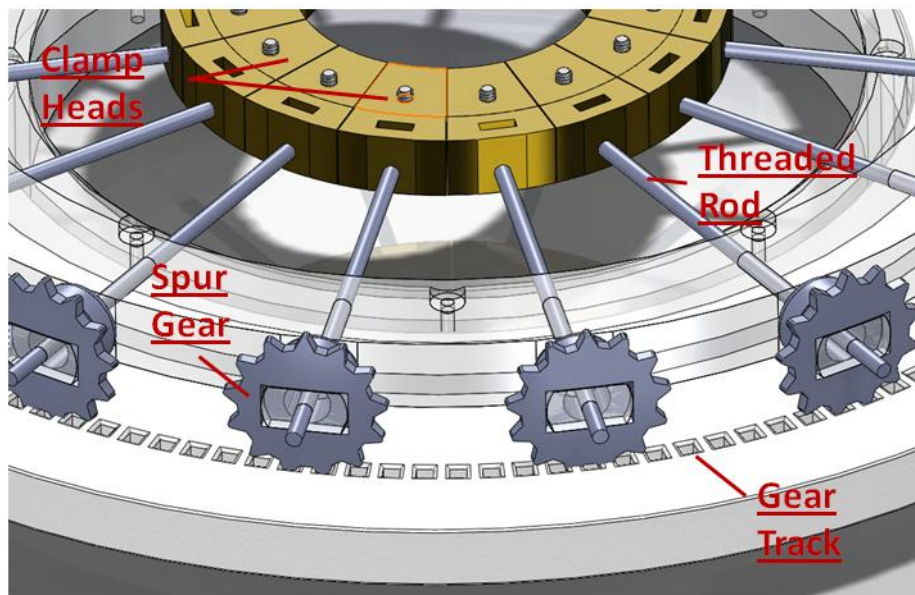


Figure 2. Basic apparatus components.

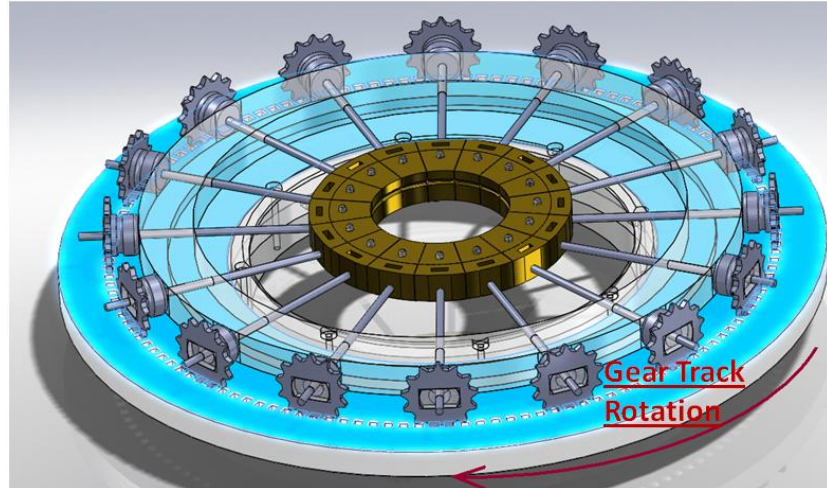


Figure 3. Gear track motion for increasing strain (shown at minimum strain, starting position).

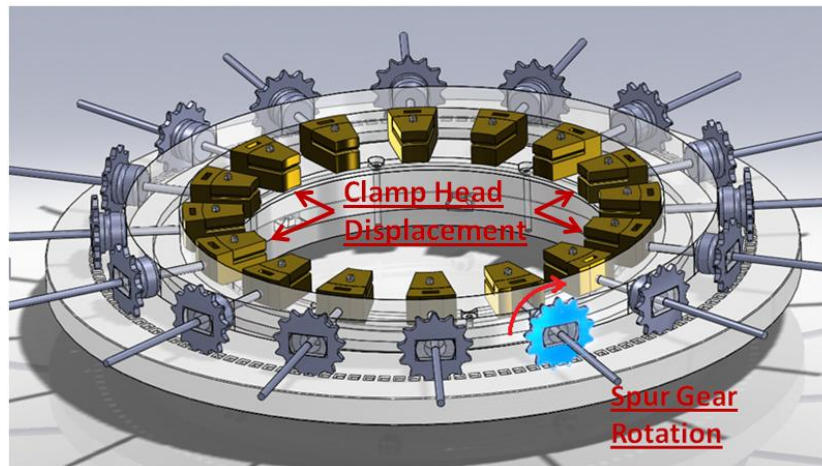


Figure 4. Spur gear rotation for increasing strain and corresponding clamp head displacement (shown at maximum strain).

We have achieved a large range for applied strain (greater than 625% change in area) in the apparatus as-built. The choice of sample starting radius determines both the maximum achievable strain and the resolution at which the strain can be applied. The larger the strain range, the lower the resolution. For this reason, the starting radius for the sample must be carefully considered. The mathematical relationship between range and accuracy of the applied strain is described later in this section of this report.

We determined that the relatively compact apparatus needed 16 clamp heads. The number 16 was determined empirically to be the minimum number required to avoid too great an influence of Poisson's effect on the deformed membrane shape under high-strain conditions. The number of clamp heads that is practical to implement is limited by the surrounding structural geometry.

Thus, the number of clamp heads represents a compromise between strain uniformity and utility of operation. Saint-Venant's principle tells us that given a sufficient distance away from a nonuniform boundary condition, the effect of the nonuniformity becomes negligible and disappears in the material state (Love, 1927; Von Mises, 1945; Saint-Venant, 1855). Adequate uniformity of the prestrain condition is thus achieved by limiting the region of interest of the prestrained membrane to a fraction of the overall radius of the membrane. The images in figure 5 compare Poisson's effect with 8 and 16 clamp heads. The range and uniformity of the strain condition are further discussed in section 3 of this report.

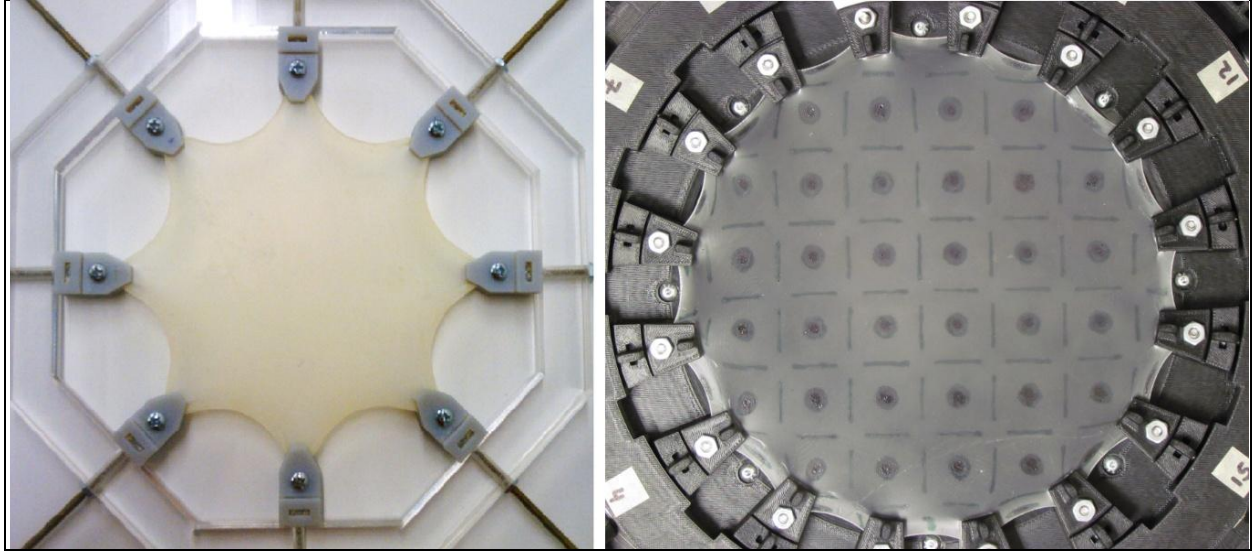


Figure 5. Comparison of Poisson's effect for eight clamp heads (left) and sixteen clamp heads (right).

The apparatus geometry and the related performance capabilities are calculated using the following mathematical relations. The desired strain (ϵ) is defined as the area strain applied to the membrane, which is given by:

$$\epsilon = (A_\epsilon - A_0) / A_0 = A_\epsilon / A_0 - 1. \quad (1)$$

The nominal, or starting, area of the membrane is represented by A_0 , while the strained membrane area is represented by A_ϵ , where

$$A_\epsilon = \pi r_\epsilon^2. \quad (2)$$

$$A_0 = \pi r_0^2. \quad (3)$$

The relationship between the radius of the strained circular sample (r_ϵ) necessary to achieve the desired prestrain (ϵ) and the nominal (starting) membrane radius (r_0) is thus calculated as

$$r_\epsilon = \sqrt{(\epsilon + 1)r_0^2}. \quad (4)$$

The membrane radius is defined as the distance from the center of the membrane out to the inner face of the clamp head, and the membrane diameter as the distance between opposite clamp head faces. The minimum (r_{min}) and maximum (r_{max}) membrane radii that the apparatus can achieve as-built are indicated as

$$r_{min} = 31.55 \text{ mm} . \quad (5)$$

$$r_{max} = 85.72 \text{ mm} . \quad (6)$$

An arbitrary starting membrane radius is indicated by its percentage of the range between r_{min} and r_{max} . For example, a 25% range would be calculated thus:

$$r_{25\%} = r_{min} + 0.25(r_{max} - r_{min}) = 45.09 \text{ mm} . \quad (7)$$

Figure 3 shows the minimum radius for the apparatus, whereas in figure 4, the constraint is provided by the clearance distance between the back of the clamp head and the inner radius of the fixture mounting ring. This clearance distance is represented by (D_r), as shown in Figure 6:

$$D_r = R - r_{\epsilon} - L_h \geq 0 . \quad (8)$$

$$D_{r_{min}} = R - r_{max} - L_h = 0 \text{ mm} . \quad (9)$$

$$D_{r_{max}} = R - r_{min} - L_h = 54.17 \text{ mm} . \quad (10)$$

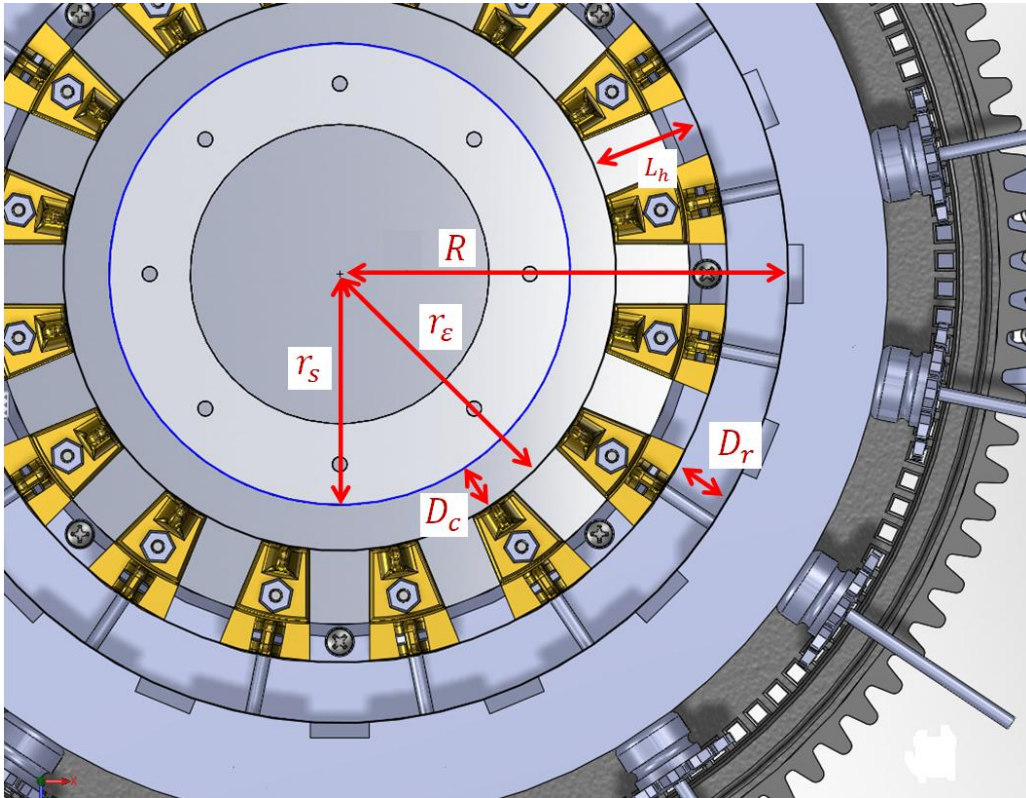


Figure 6. Apparatus top view including slide mount (ring at center) with significant dimensions and limits called out.

The inner radius of the fixture mounting ring (R) is 114.3 mm. The clamp head length (L_h) is 28.58 mm. $D_{r_{max}}$ represents the maximum head travel allowed by the geometric constraints of the apparatus, knowledge of which is necessary when setting software operating limits in the apparatus interface software.

When the prestrained sample is to be mounted to a rigid substrate, or “slide mount,” an operational constraint also arises from the requirement for some nominal clearance distance (D_c) between the outer circumference of the slide mount and the inner circumference of the clamp head, which is given by:

$$D_c = r_\varepsilon - r_s \geq 0 . \quad (11)$$

The outer radius of the standard slide mount (r_s) is 59.06 mm. It is important that the front head clearance be sufficient in order to fit and bond the mounting slide to the strained membrane should removal from the apparatus be required for performing additional tests on the sample.

The radial head displacement (D_h) that is required to yield a desired prestrain is given by

$$D_h = r_\varepsilon - r_0 . \quad (12)$$

The nominal radius of the membrane samples, as measured as one-half the distance between opposing clamp heads before strain is applied, determines what the final strain will be for a given radial displacement. It is possible with the apparatus to choose an arbitrary nominal radius subject to the constraint $r_{min} \leq r_0 \leq r_{max}$. Knowing both the nominal and final radii to a high degree of confidence is important in order to have confidence in the final applied strain value; this confidence follows correct operation of the apparatus.

The apparatus is operated through computer control of stepper motors. The stepper motors have a gear head that is meshed to the gear track, which itself is a large circular gear. The stepper motor rotates, rotating the gear track, which rotates the spur gear, which causes the threaded rod to translate in and out, thus inducing a radial displacement of the clamp head. The fundamental relationship that is of interest to the operator is, therefore, the resulting applied strain (ε) as a function of the number of steps that the motor rotates (N). Derivation of this fundamental relationship follows. The gear ratio (C) for the apparatus is a function of the number of gear teeth on the stepper motor gear head ($C_g = 10$), the number of teeth on the spur gear ($C_s = 13$), the number of holes in the gear track circumference ($T_h = 136$), and the number of teeth around the perimeter of the gear track ($T_t = 110$), and is calculated as

$$C = C_g T_h / T_t C_s . \quad (13)$$

The screw pitch (linear displacement per revolution of spur gear) is ($P = 0.6091$ mm). The number of steps per 360° rotation of the stepper motor is (N_M). Therefore, the radial head displacement per motor step (D_N) can be calculated as follows:

$$D_N = CP/N_M = C_g T_h P / T_t C_s N_M . \quad (14)$$

The theoretical head displacement per step for the as-designed apparatus is calculated to be $\sim 0.28964 \mu\text{m}$ per stepper motor step, assuming microstepping is enabled, yielding 2000 steps per motor revolution. This value is in good agreement with the experimentally measured value for the as-built displacement of $0.28997 \mu\text{m}$ per motor step. The actual radial head displacement (D_h) for N steps is then given by

$$D_h = ND_N . \quad (15)$$

Examining equations 1–3 and 11, the following relationship for applied area strain (ε) is revealed:

$$\varepsilon = (r_0 + D_h)^2 / r_0^2 - 1 . \quad (16)$$

This further reduces to

$$\varepsilon = \frac{D_h}{r_0} \left(\frac{D_h}{r_0} + 2 \right) . \quad (17)$$

The strain envelope of the apparatus is shown in figure 7.

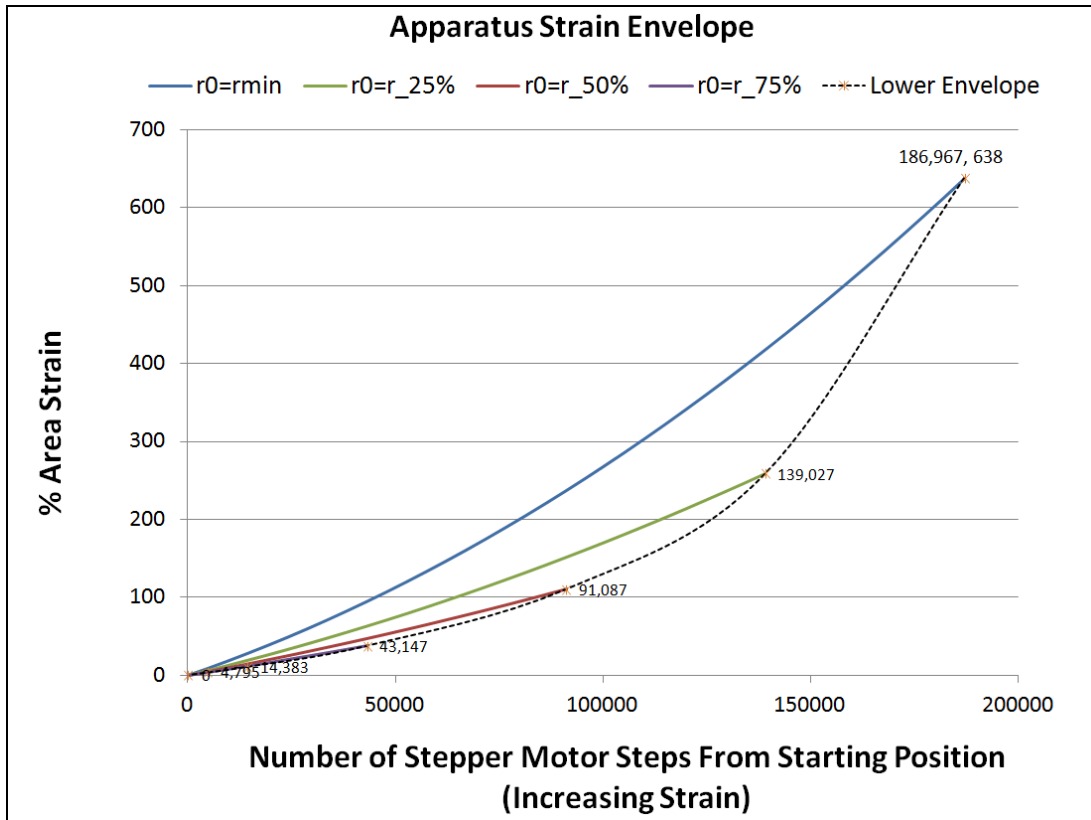


Figure 7. The relationship between desired area strain values and the number of motor steps required to achieve the desired strain is shown for the as-designed apparatus.

Note: Achievable values are indicated in the bounded region. The slope and maximum achievable strain are both shown to vary with starting radius.

The resolution of the apparatus (ε_N), as measured in strain per step, is a function of both the starting radius and the distance the clamp head has already traveled away from the starting radius. The resolution is, therefore, not a constant for a given starting radius. The resolution is calculated as follows:

$$\varepsilon_N = \varepsilon / N = \frac{D_N}{r_0} \left(\frac{ND_N}{r_0} + 2 \right). \quad (19)$$

Figure 8 shows the resolution envelope for the apparatus as-built. The strain resolution per stepper motor step is shown to be always better than 0.0034% (34 μ strain) area strain per step, or 6.8% area strain per revolution of the stepper motor, equivalent to 2000 steps. For best precision, the user should select as large a starting radius as possible so as to achieve the maximum resolution.

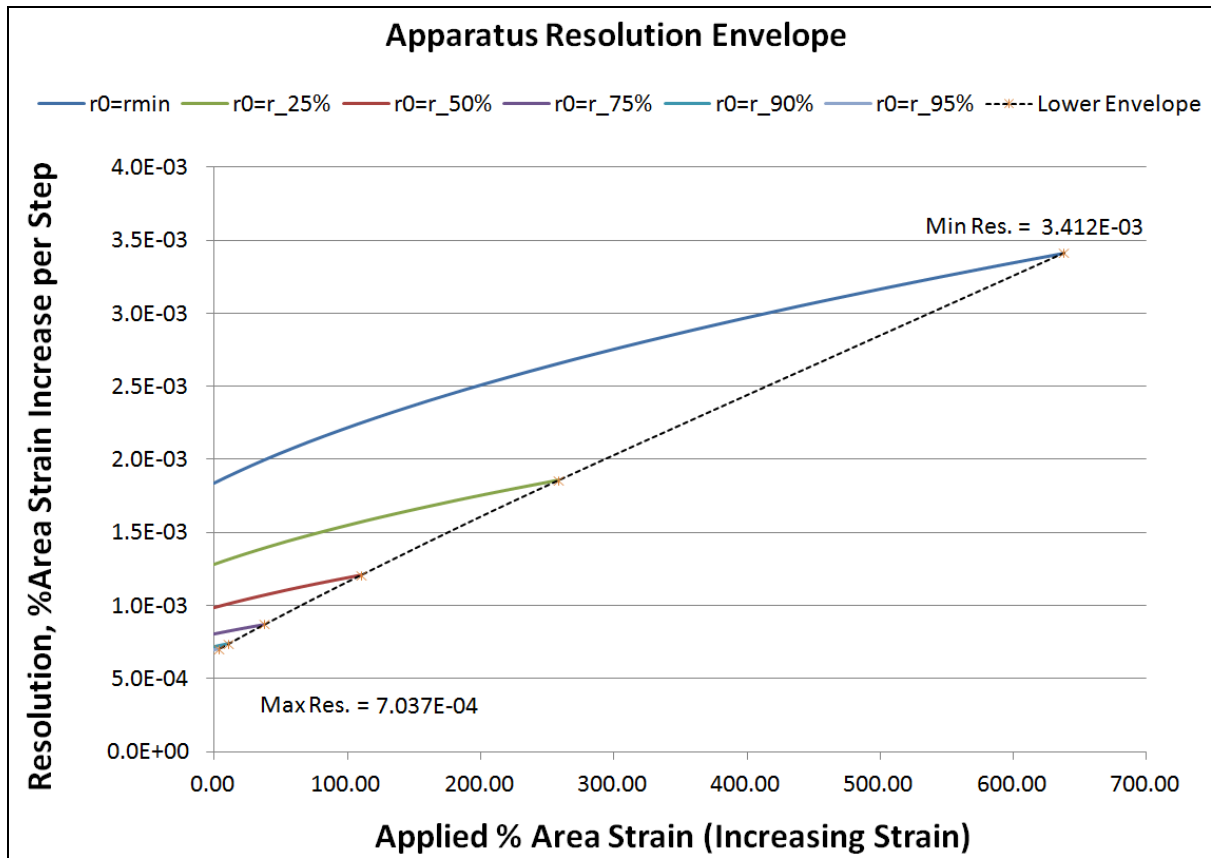


Figure 8. The as-built envelope for resolution, assuming microstepping is used.

Note: Only resolutions at achievable levels of strain for each starting radius are indicated. The bounded region thus indicates attainable values for the as-built device.

2.2 Significant Features

During the iterative development process for this apparatus, we identified a number of operational considerations. The most significant operational considerations and their respective solutions are described in the following sections.

2.2.1 Shaft Encoders

Shaft encoders provide a convenient feedback mechanism for closed-loop control of rotary positioning devices, such as stepper motors. Open-loop control of stepper motors is often adequate, provided the torque limit of the stepper motor will not be approached or exceeded. Should the torque limit be exceeded, even briefly, the commanded step displacements may not be executed, which leads to under actuation. Shaft encoders allow missed step executions to be identified and corrected with a closed-loop software implementation. A secondary shaft encoder was deemed desirable for the strain apparatus since stiff specimens, which would have the potential to briefly overload the stepper motors, may be considered. Two encoders placed at different operational points in the apparatus drive serve as a diagnostic tool to identify potential malfunctions and help isolate their potential cause.

The primary shaft encoder (figure 9, left) is directly connected to the drive shaft of the stepper motor and provides direct feedback for motor rotational displacement. The secondary shaft encoder (figure 9, right) provides direct feedback for spur gear rotational displacement. The secondary shaft encoder was designed to be easily removed in order to service the apparatus or to accommodate specific experiments.

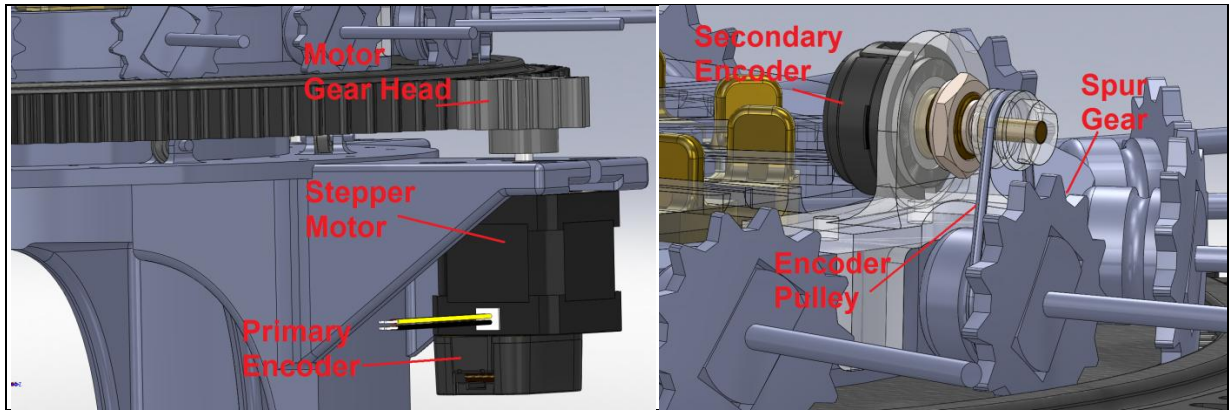


Figure 9. Primary motor encoder (left) and secondary shaft encoder (right) placements.

The primary shaft encoder outputs ($S1_{360} = 500$) pulses per full revolution. Thus the strain resolution (ϵ_{S1}) per primary shaft encoder pulse (N_{S1}) is given as

$$\epsilon_{S1} = \epsilon / N_{S1} = \frac{D_{S1}}{r_0} \left(\frac{N_{S1} D_{S1}}{r_0} + 2 \right), \quad (20)$$

where

$$D_{S1} = D_h N_M / S1_{360}. \quad (21)$$

The secondary shaft encoder is rotated by motion of the spur gear through a 1:2 increase pulley. The secondary shaft encoder outputs ($S2_{360} = 300$) pulses per full revolution. Thus the strain per secondary shaft encoder pulse (N_{S2}) is given as

$$\varepsilon_{S2} = \varepsilon / N_{S2} = \frac{D_{S2}}{r_0} \left(\frac{N_{S2} D_{S2}}{r_0} + 2 \right), \quad (22)$$

where

$$D_{S2} = P / 2S2_{360}. \quad (23)$$

2.2.2 Clamp Design (Jaw Shape and Screw-Down Method)

The geometry of the clamping mechanism impacts the strain gradient in the immediate vicinity of the clamp. Thus, for high levels of applied strain, the clamp geometry has a significant impact on the likelihood of the sample to tear. To alleviate sample tearing, we designed a specific clamping geometry that also provides adequate sample holding capability to avoid slipping. The geometry of the upper clamp was customized, whereas the bottom surface of the clamp was left planar. Figure 10 shows the upper clamp geometry that was customized to alleviate large strain gradients and associated tearing of the sample in the vicinity of the clamp head.

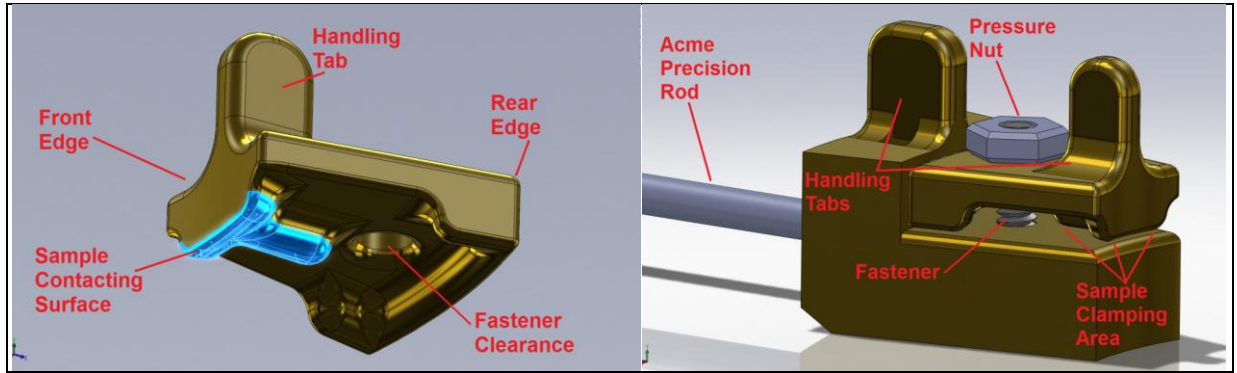


Figure 10. Upper clamp geometry (highlighted, left) and clamp head assembly showing clamping and handling features (right).

Figure 10 also shows the entire clamp head assembly. The upper clamp is lowered onto the sample and properly aligned using the handling tab. The pressure nut is then screwed down until an adequate clamping pressure is achieved.

2.2.3 Antitwist Cover

Small amounts of friction between the precision nuts and the precision acme rods can lead to the clamp heads rotating during increasing or decreasing strain operations if they are not physically constrained. Clamp head rotation is undesirable, as it prevents an accurate strain state from being known under quasi-statically and dynamically applied deformations. To prevent the heads from rotating during operation, we implemented a removable antitwist cover. Slots in the antitwist cover guide the handling tabs on the clamp heads and prevent the heads from rotating. The cover is shown in figure 11.

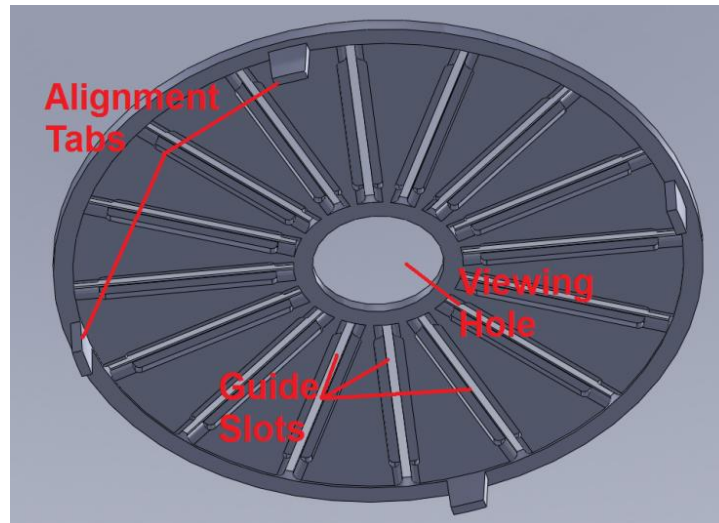


Figure 11. Antitwist cover with major features labeled.

The antitwist cover is placed on the apparatus using the alignment tabs and can be easily removed for sample removal or experimentation. The cover is shown in use on the apparatus in figure 12.

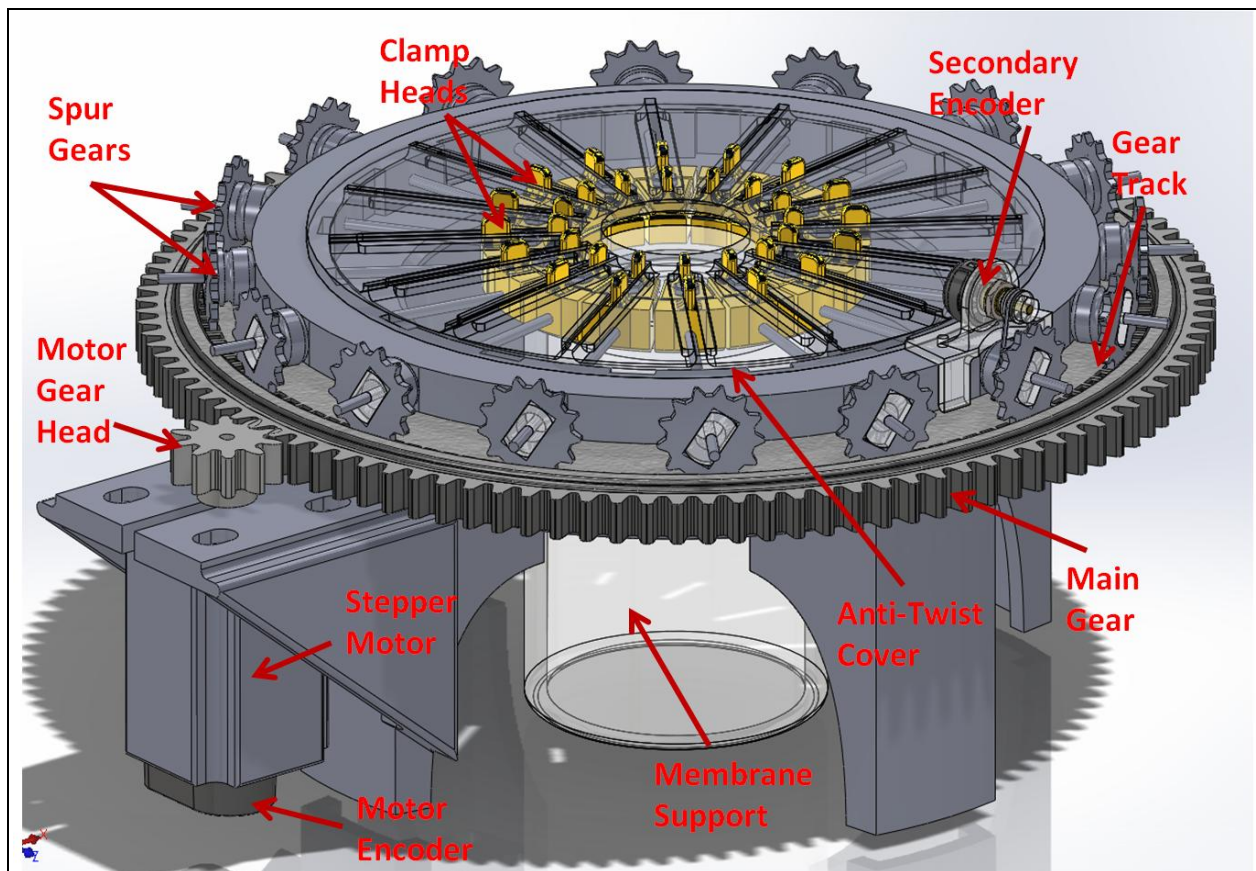


Figure 12. Final design embodiment of the apparatus.

2.2.4 Electrical Interfaces for In Situ Electrical Characterization

Electrical contact with the sample upper or lower surfaces can be provided independently via purpose-built conducting clamp heads. Insulating plastic clamp head components can be swapped out for metallic conductive components, as shown in figure 13.

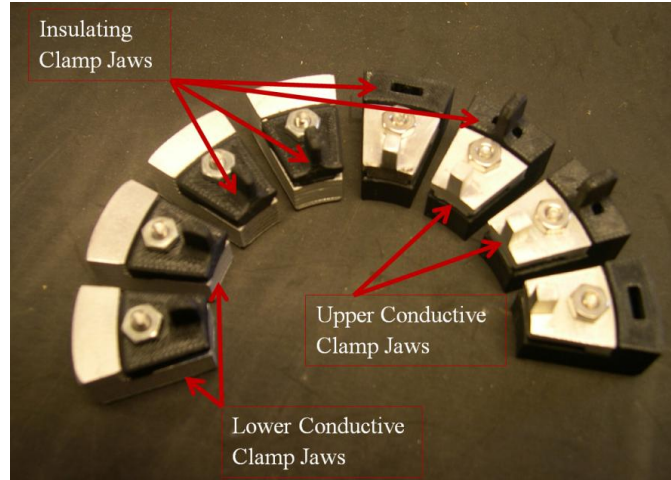


Figure 13. Conducting clamp components for electrical interface to a specimen.

The upper and lower clamp jaws can be replaced with conductive components either independently or in tandem. Any number of combinations is possible up to and including replacing all 16 plastic clamp heads. Figure 14 shows two typical configurations: one used for making in situ four-wire conductivity measurements (left image) and another for measuring change in capacitance with applied area strain for a compliant capacitor (right image).

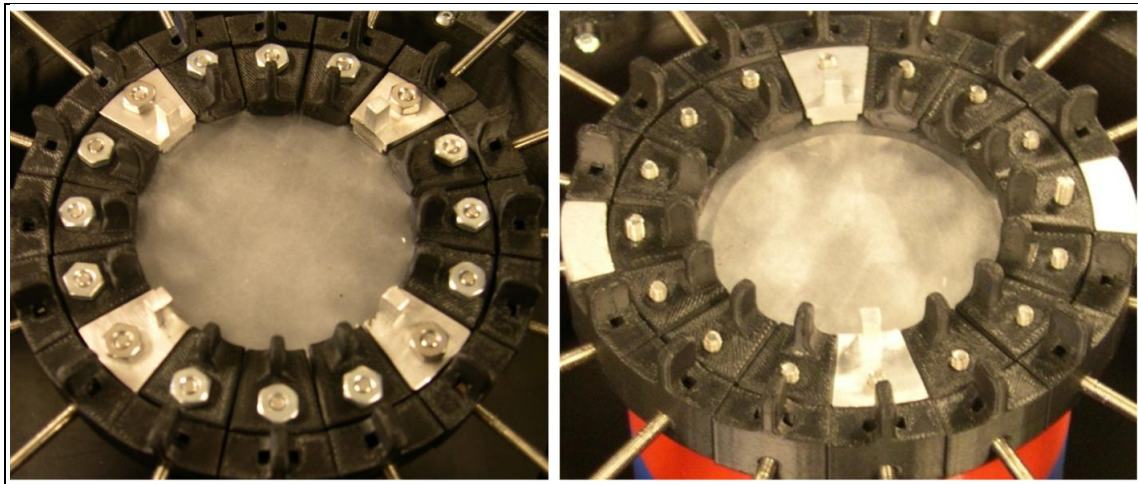


Figure 14. Two typical configurations for characterizing shift in electrical properties with large biaxial strain: upper clamp jaw configuration for four-wire conductivity measurements (left) and dual upper/lower jaw configuration for measurement of capacitance on a hyperelastic compliant capacitor (right).

3. Validation and Performance Assessment

In order to establish confidence in the as-built device for purposes of publishing data, we performed three different experimental characterizations of the device. First, a laser displacement sensor was used to verify that the displacement per motor encoder pulse is in good agreement with the designed value. The designed value of head displacement per motor encoder pulse was $1.1585\text{ }\mu\text{m}$ per encoder pulse. The experimentally determined value for the as-built device was $1.1598\text{ }\mu\text{m}$ per encoder pulse. The same characterization method also revealed a head-to-head variability in displacement/pulse of less than $\pm 0.1\%$. Second, a photographic method was used to validate that the theoretically applied strain agrees with the resulting strain measured on the circular membrane. Third, a digital image correlation (DIC) technique was used to validate the assumption that the strain is applied uniformly over the membrane area. Additional description and details for the results of each method of performance assessment is included in the following sections.

3.1 Validation of Uniform Head Displacement

A Microtrak LTC-200-100 laser displacement sensor was used to measure variability in displacement between each of the 16 heads. Multiple runs were performed for each head, and curves were fit to the data for millimeter displacement vs. number of motor encoder pulses. Figure 15 shows a representative curve fit for a single head. Figure 16 shows the resulting variability between each head, measured in terms of percent difference from the average slope.

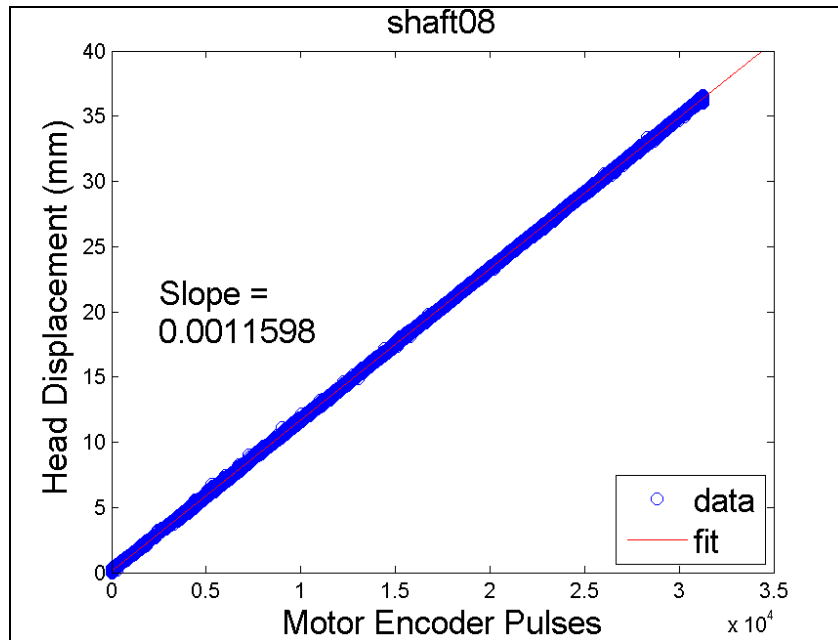


Figure 15. Representative data of head displacement curve fitting using the laser displacement sensor.

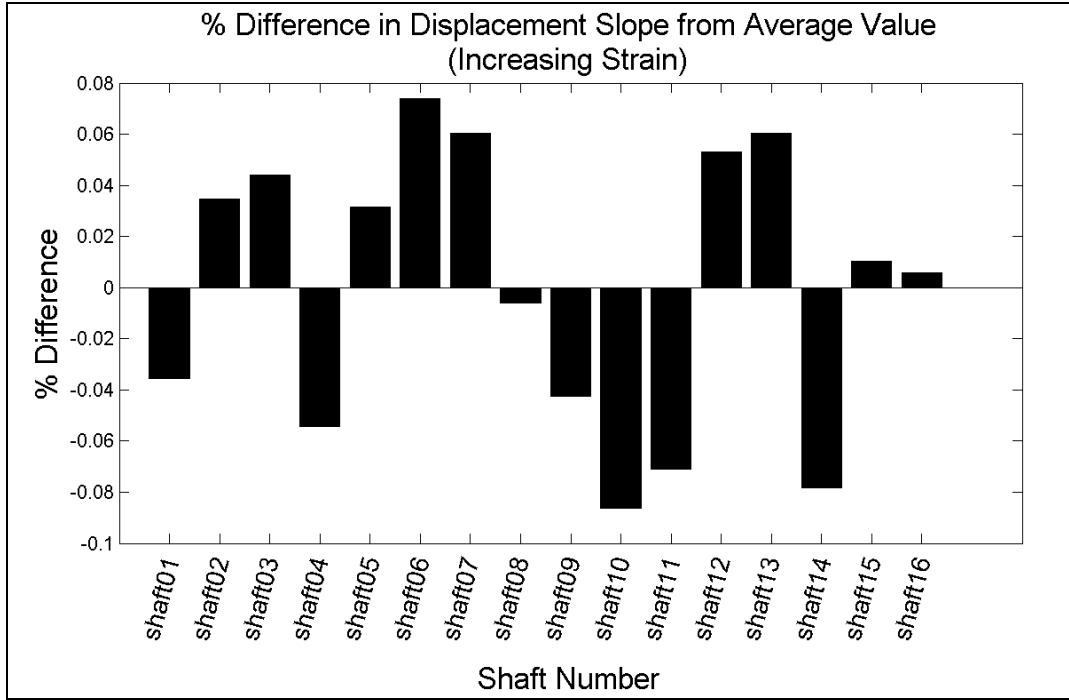


Figure 16. Cross-head variability from average displacement slope for each of the 16 heads.

Average head displacement was experimentally determined to be equal to 0.001159870 mm per motor encoder pulse, which translates to 0.00028997-mm displacement per stepper motor step, or slightly less than 0.3 μm of head displacement per stepper motor step. This assumes 2000 steps per full revolution of the stepper motor, or 0.18° per step, and 500 motor encoder pulses per motor revolution. Cross-head variability in slope was determined to be less than $\pm 0.1\%$ in all cases. Both results lend a high degree of confidence in the device reliability and repeatability. Additional confidence is gained when one considers that the magnitude of the cross-head variability measurements was close to the noise floor of the laser displacement sensor used to measure head displacement, leading the author to conclude that at least some of the measured cross-head variability can be attributed to sensor noise.

3.2 Photographic Validation of Applied Strain

In order to validate the assumption that the commanded strain is the same as the actual resultant strain on the membrane sample, a photographic method was used. A geometric pattern was drawn onto a membrane sample at zero strain. The membrane sample was then clamped into the apparatus. A series of images were taken at various commanded strain values. Strain was measured at the center of the sample for each commanded strain value using an image-processing technique. The feature pixel centroid location of each of four points (A, B, C, D) defining an area on the membrane was recorded in each image, as depicted in figure 17.

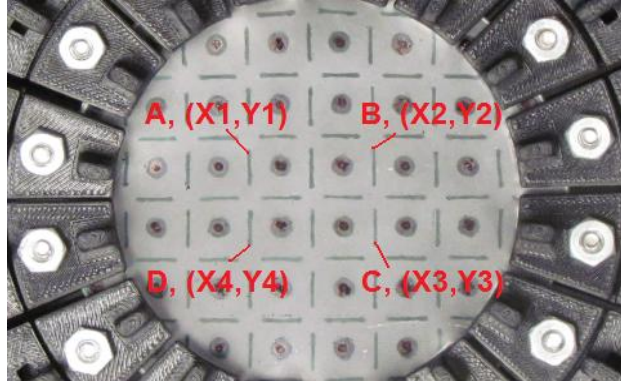


Figure 17. Photo measurement grid.

The area defined by the four points was calculated and compared with the commanded strain values, as shown in figure 18. Error bounds represent worst-case scenarios for calculating photo-measured strain values. Worst-cases occur when far outside (upper bound) or inside (lower bound) pixels are selected rather than the center pixel for the centroids of each point in the image-processing algorithm. Figure 18 also includes theoretically maximum upper and lower error bounds, which are defined by the worst-case scenarios of pixel selection for feature centroid, as depicted in figure 19.

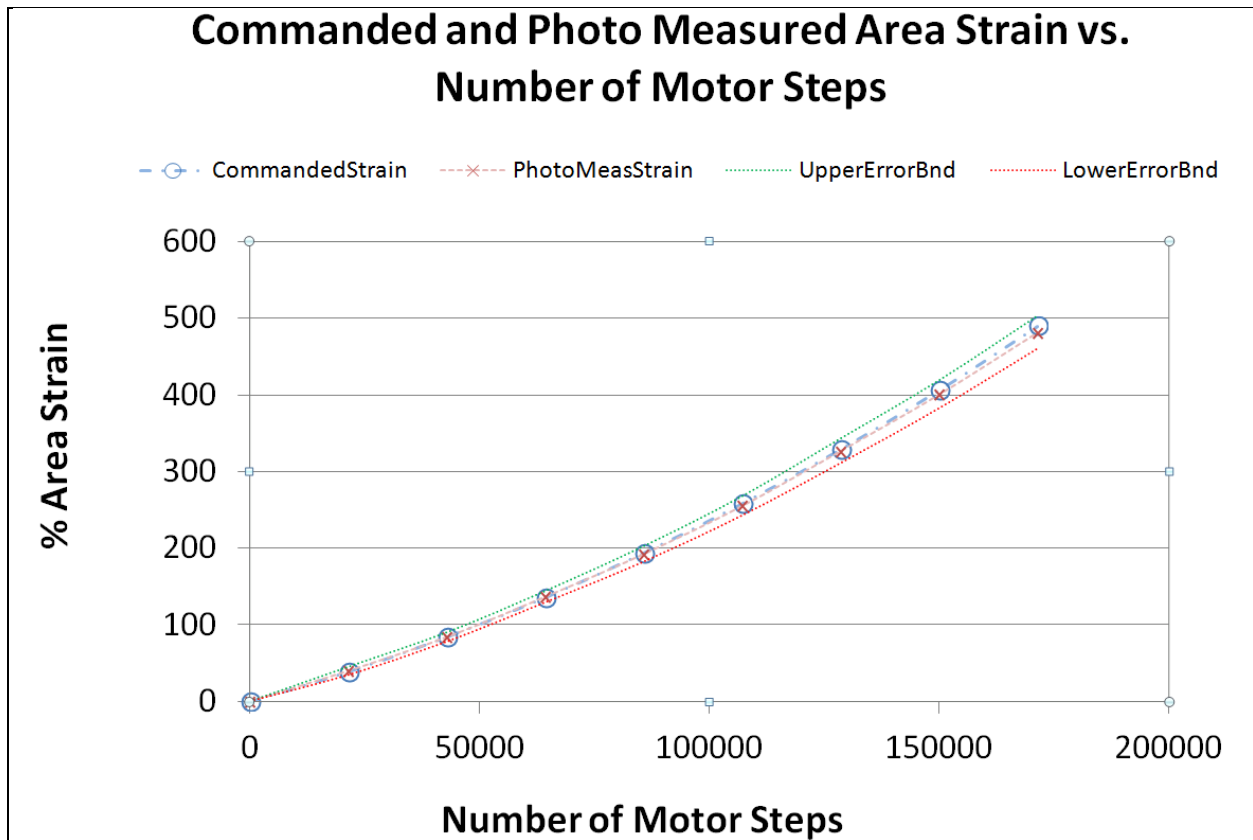


Figure 18. Overlay of photo-measured strain data and predicted strain values vs. number of stepper motor steps.

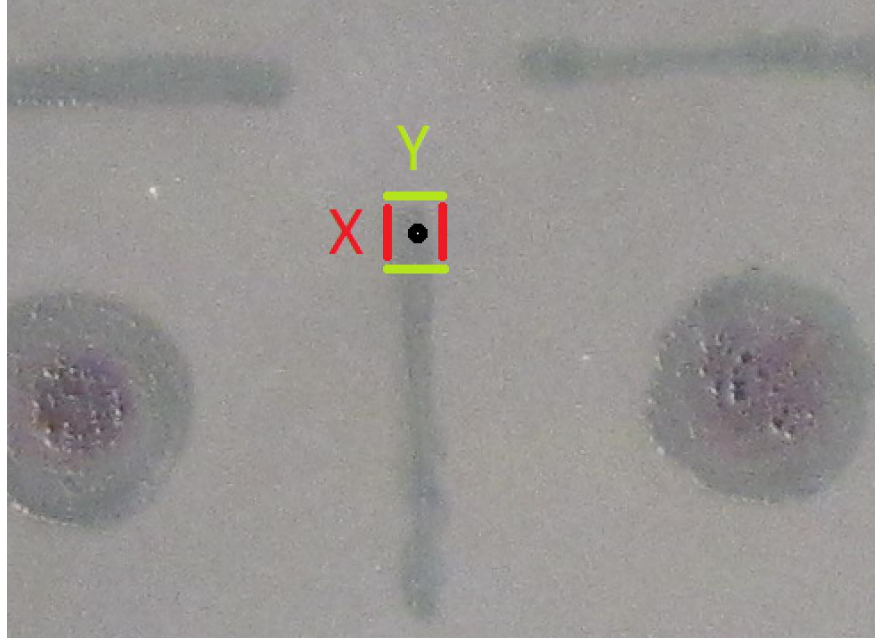


Figure 19. Zoomed in from figure 17, example of worst-case bounds on pixel selection for the centroid of a point (indicated by black dot) in the image-processing algorithm.

The results from the photographic measurement technique shown in figure 18 confirm that the resultant strain on the membrane agrees well with the commanded strain, within the limits of the photographic measurement technique.

3.3 Validation of Strain Uniformity Using DIC

DIC was used to verify that uniform strain is being applied to the isotropic membrane sample. A speckle pattern was applied to the membrane sample at zero strain. A series of images were taken of increasing strain values under strongly backlit lighting conditions using a digital camera rigidly mounted to a tripod a fixed distance above the membrane plane. Images were processed into black and white using MATLAB. The software package, VIC-3D (from CorrelatedSolutions), was used to process the images and measure the resulting strain field. A representative sample of the processed images with the uniform strain field overlaid can be seen in figure 20.

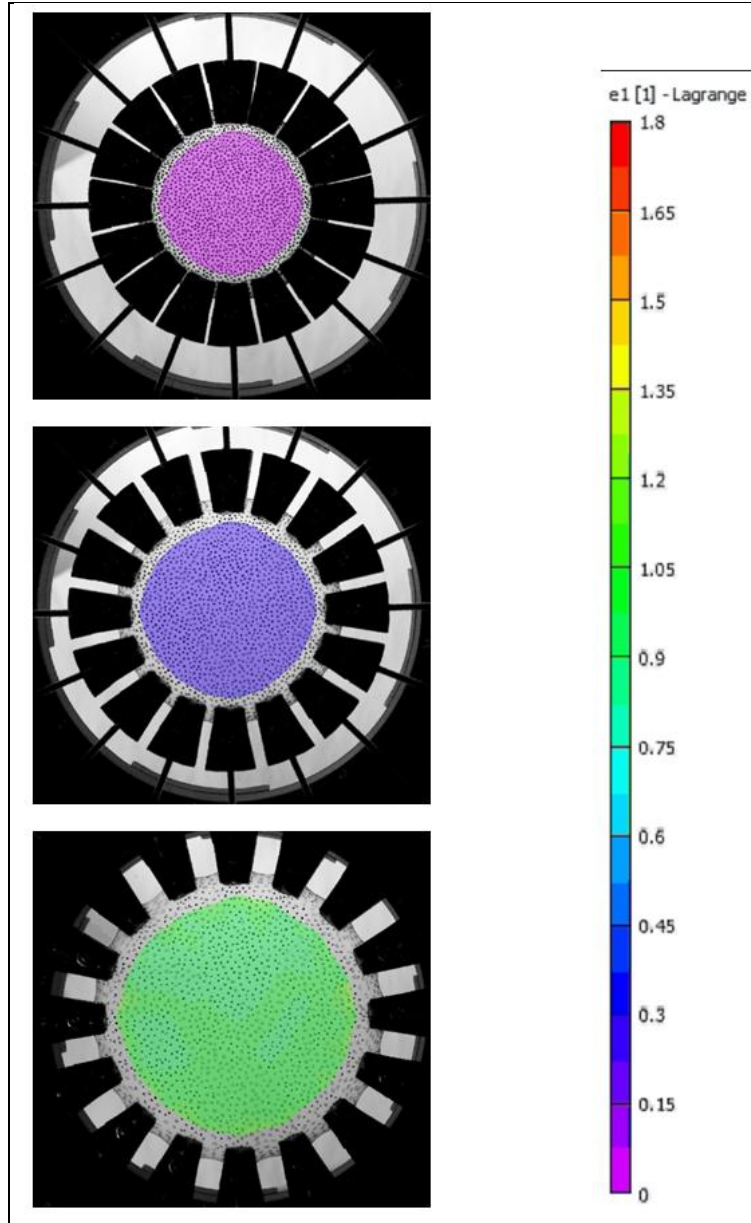


Figure 20. DIC results showing uniform strain distribution for (from top to bottom) 0%, 150%, and 400% area strains.

4. Conclusions

The design and performance of an apparatus capable of applying large (greater than 625% area strain), precisely controlled (better than 0.003% area strain resolution) equi-biaxial strains to thin circular membrane samples has been presented. A high degree of confidence in the reliability and repeatability of the as-built apparatus has been gained through rigorous experimental

performance assessment. The apparatus can be used for performing electromechanical characterizations of membrane samples or for preparing samples through application of large pre-strains for further experimentation (e.g., dielectric spectroscopy or scanning electron microscopy [SEM] analysis post-strain). The device concept described in this report can be readily scaled either up or down for adaptation to other experimental infrastructure (e.g., equi-biaxial strain application inside a SEM chamber).

5. References

- Jean-Mistral, C.; Sylvestre, A.; Basrour, S.; Chaillout, J.-J. Dielectric Properties of Polyacrylate Thick Films Used in Sensors and Actuators. *Smart Materials and Structures* **2010**, *19* (075019), 9.
- Love, A. E. H. *A Treatise on the Mathematical Theory of Elasticity*; Cambridge University Press: New York, 1927.
- Rivlin, R. S.; Saunders, D. W. Large Elastic Deformations of Isotropic Materials VII. Experiments on the Deformation of Rubber. In *Collected Papers of R. S. Rivlin Vol. I*; Barenblatt, G. I., Joseph, D. D., Eds.; Springer-Verlag: New York, 1997.
- Saint-Venant, A. J. C. B. Memoire sur la Torsion des Prismes. *Mem. Divers Savants* **1855**, *14*, 233–560.
- Slipher, G.; Mrozek, R.; Shumaker, J. Tunable Band-Pass Filters Employing Stretchable Electronic Components. *Proceedings of the ASME 2012 Conference on Smart Materials, Adaptive Structures and Intelligent Systems*, Stone Mountain, GA, 2012.
- Treloar, L. R. G. Stresses and Birefringence in Rubber Subjected to General Homogeneous Strain. *Proc. Phys. Soc.* **1948**, *60*, 135.
- Von Mises, R. On Saint-Venant's Principle. *Bulletin AMS* **1945**, *51*, 555–562.

NO. OF
COPIES ORGANIZATION

1 DEFENSE TECHNICAL
(PDF) INFORMATION CTR
DTIC OCA

1 DIRECTOR
(PDF) US ARMY RESEARCH LAB
RDRL CIO LL

1 GOVT PRINTG OFC
(PDF) A MALHOTRA

1 RDRL VTA
(PDF) G SLIPHER

INTENTIONALLY LEFT BLANK.